SCIENCE CHINA
Technological Sciences

Special Topic: Impact Dynamics of Structures/Materials
•Article•

July 2021 Vol.64 No.7: 1360–1370
https://doi.org/10.1007/s11431-021-1814-y

# Atomic-level mechanism of spallation microvoid nucleation in medium entropy alloys under shock loading

XIE ZhouCan[1,2], CHEN Yan[1,2*], WANG HaiYing[1,2] & DAI LanHong[1,2,3*]

[1] *State Key Laboratory of Nonlinear Mechanics, Institute of Mechanics, Chinese Academy of Sciences, Beijing 100190, China;*
[2] *School of Engineering Science, University of Chinese Academy of Sciences, Beijing 101408, China;*
[3] *State Key Laboratory of Explosion Science and Technology, Beijing Institute of Technology, Beijing 100081, China*

Received January 10, 2021; accepted March 18, 2021; published online June 15, 2021

Spallation, rupture under impulsive tensile loading, is a dynamic failure process involving the collective evolution and accumulation of enormous microdamage in solids. In contrast to traditional alloys, the spallation mechanism in medium entropy alloys, the recently emerged multiprinciple and chemically disordered alloys, is poorly understood. Here we conduct molecular dynamics simulations and first principle calculations to investigate the effects of impact velocities and the local chemical order on spallation microvoid nucleation in a CrCoNi medium entropy alloy under shock wave loading. As the impact velocity increases, the microvoid nucleation site exhibits a transition from the grain boundaries to the grains to release redundant imposed energy. During the intragranular nucleation process, microvoids nucleate in the poor-Cr region with a large local nonaffine deformation, which is attributed to the weak metallic bonds in this position with sparse free electrons. For intergranular nucleation, a Franke-like dislocation source forms through the dislocation reaction, leading to enormous dislocations piling up in a narrow twin stripe, which markedly increases the local stored energy and promotes microvoid nucleation. These results shed light on the mechanism of spallation in chemically complexed medium entropy alloys.

**high/medium entropy alloys, spallation, microvoid nucleation, chemical order**

**Citation:** Xie Z C, Chen Y, Wang H Y, et al. Atomic-level mechanism of spallation microvoid nucleation in medium entropy alloys under shock loading. Sci China Tech Sci, 2021, 64: 1360–1370, https://doi.org/10.1007/s11431-021-1814-y

## 1 Introduction

Spallation, a typical instantaneous dynamic fracture mode, is triggered by tensile stress due to the interaction between rarefaction waves [1–3] and usually occurs in many engineering fields, such as explosions [4] and penetrations [5–7]. It is a trans-scale dynamic process that includes the collective evolution of numerous microscopic voids or cracks [8,9]. Based on extensive measurements of the microdamage population in spallation, Curran et al. [2] proposed a nucleation and growth model with mesoscopic kinetics of microvoids. Microvoid nucleation is mainly attributed to three parts: thermally-activated diffusional process [10,11], debonding at the second-phase interface as the stress progressively increases [12], and cavitation due to plastic strain accumulation [13,14]. The growth of microvoids is mainly attributed to plastic deformation of the matrix [15–18]. Furthermore, Bai et al. [3,8] established the statistical evolution of microvoids based on the number density conservation law in a phase space. Thus, the spallation of traditional single principal alloys can be described quantitatively in combination with the framework of continuum mechanics. However, the performance and underlying mechanisms of dynamic fractures are still unclear in novel and promising medium-entropy alloys.

Recently, high/medium-entropy alloys (H/MEAs), in

*Corresponding authors (email: chenyan@lnm.imech.ac.cn; lhdai@lnm.imech.ac.cn)

which multiple principal elements in equal or near equal molar ratios are occupied randomly on topologically ordered crystallographic lattices, have emerged as an exciting new class of metallic structural materials [19–23]. This unique atom-packing structure with a high chemical disorder imparts HEAs' many extraordinary mechanical properties, such as an excellent combination of strength and ductility [21,24–28], superior performance at an extremely low temperature [29], high hydrogen and corrosion resistance [30,31], an exceptional "self-sharpening" capability [7] and shock resistance [32,33]. For example, conspicuous element aggregation provides considerable resistance to dislocation glide, which overcomes the strength and ductility trade-off [34,35]. However, the atomic-level influence of the local chemical order on microvoid nucleation in the dynamic spallation process is elusive.

In this paper, a series of molecular dynamics (MD) simulations were performed to investigate the spallation process of CrCoNi MEA at different shock velocities. The evolution of microstructures, such as dislocations, hexagonal closest packed (HCP), face-centered cubic (FCC) phases and microvoids, was surveyed. The effect of the local chemical order on the nucleation process was discussed with first principle calculation in intergranular nucleation, and elaborate descriptions from dislocation interaction to intragranular nucleation were presented.

## 2 Computational method

MD simulations were conducted using Large-scale Atomic/Molecular Massively Parallel Simulator code [36]. First, a polycrystal Ni sample with dimensions of 40 nm× 40 nm× 100 nm and ~ $1.5 \times 10^7$ atoms was generated by the Voronoi construction method using the Atomsk package [37], with an average grain size of 16 nm. The Ni atoms were replaced with Cr and Co to ensure atomic number $N_{Cr}$:$N_{Co}$:$N_{Ni}$ = 1:1:1 and the number of nearest neighbor element pairs $\delta_{Cr\text{-}Cr}$:$\delta_{Cr\text{-}Co}$:$\delta_{Cr\text{-}Ni}$:$\delta_{Co\text{-}Co}$:$\delta_{Co\text{-}Ni}$:$\delta_{Ni\text{-}Ni}$ =1:1:1:1:1:1 (Figure 1(a)) using Fortran code. During the MD simulation, the embedded-atom method potential of CrCoNi developed by Li was applied [38], which precisely describes element aggregation and the evolution features of dislocations and twins.

Before shock loading, the as-created sample was relaxed at 0 K by applying energy minimization using the conjugate gradient method under zero macroscopic stress, allowing the box size and shape to vary during the iterations. Then it gradually heated to the desired temperature (300 K) and finally relaxed in the Nose-Hoover isobaric-isothermal ensemble for 100 ps. To achieve shock-induced deformation, a sample with a thickness of 1 nm (the red block in Figure 1(a)) was chosen as the rigid piston, and the atoms in the piston

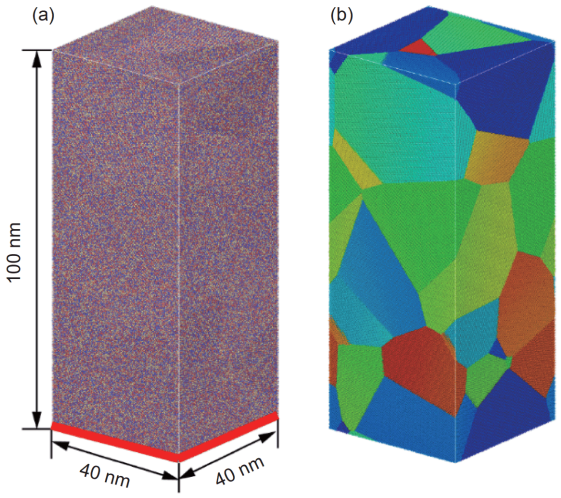


**Figure 1** (Color online) The element (a) and grain distributions (b) of the CrCoNi medium entropy alloy, respectively.

were given an initial shock velocity $U_s$ in the longitudinal direction with a duration of 12 ps. After recovering the deformation of the piston, the shock wave continued to propagate with a duration of 30 ps. Shock simulations were performed in the microcanonical NVE ensemble, and periodic boundary conditions were used in the other directions. The time step for integrating the equations of motion was 1 fs.

To investigate the dynamic fracture of the MEA, different shock velocities of 400, 600, 800, and 1000 m/s were chosen. We divided the simulation cell into fine bins along the shock direction, and the average physical properties were obtained within each bin, such as the density, stress tensor and particle velocity profiles. The atomic Mises strain, volumetric strain, local nonaffine deformation ($D^2_{min}$) [39] and rotation angle were calculated and visualized using OVITO software [40]. The characterizations of defects (stacking faults, twins, and voids) were performed using common neighbor analysis [41], construct surface mesh [42] and dislocation extraction algorithm [43].

## 3 Results and discussion

### 3.1 Spall strength

As shown in Figure 2(a), the first shock wave reaches the rear free surface at the time of point A. The plastic wave (AB) develops into a stable shock (BC), and the arrival of a release wave leads to a velocity drop (CD). Finally, the increase in the ensuing velocity (DE) is induced by a compression wave, which is reflected from the spalled plane in the sample. There are obvious spallation signs in all of the shock simulations, except for 400 m/s. The spall strength of the MEA can be deduced from the free surface velocity $U_{fs}$ as [9]

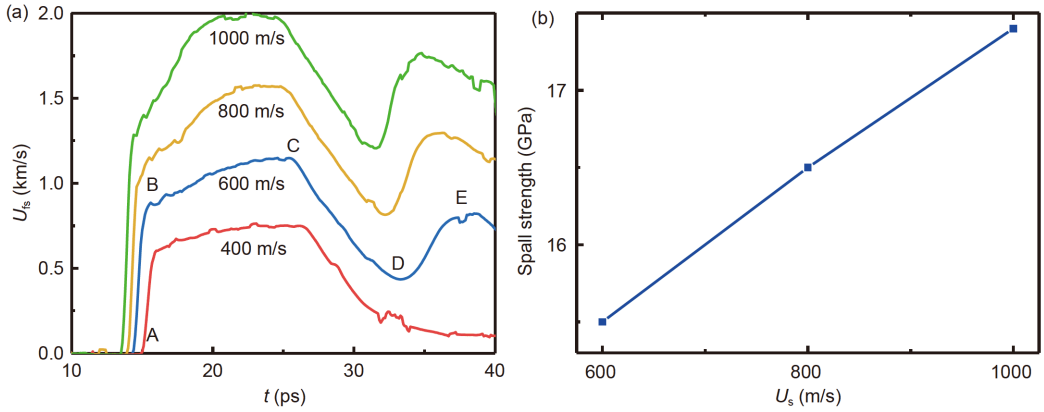


**Figure 2** The velocity profiles of the rear free surface (a) and the spall strength (b) for different impact velocities, respectively.

$$\sigma_{sp} = \frac{1}{2}\rho_0 C_b (U_C - U_D), \quad (1)$$

where $\rho_0$ is the density of the material, $C_b$ is the bulk sound speed, and $U_C$ and $U_D$ are the maximum and minimum velocities defined at points C and D, respectively. As shown in Figure 2(b), the spall strength increases with an increasing impact velocity, exhibiting a significant strain rate strengthening effect.

### 3.2 Microstructural evolution

Here we chose the case of $U_s$ = 600 m/s as an example to investigate the microstructural evolution. As shown in Figure 3(e), the peak stress behind the shock wave front reaches 48.9 GPa at $t$ = 10 ps and greatly exceeds the Hugoniot elastic limit of the MEA. Thus, the sample exhibits visible plasticity by emitting dislocations and stacking faults at the grain boundaries (see Figure 3(b)), which releases excess stress and provides a large atomic displacement. At $t$ = 12 ps, a rarefaction wave is released on the front free surface due to the recovering deformability of the piston. In addition, the shock wave reaches the rear free surface at 15 ps and is transformed into another rarefaction wave. Figure 3(c) shows that a large number of stacking faults exist in the middle zone of the sample, and its content near the free surface is relatively low. This is because both the HCP structures in the upper and lower regions are transformed back to the original FCC phase due to the propagation of rarefaction waves. Finally, a tensile zone in the sample is created by the interaction of two rarefaction waves. When the tensile stress exceeds the dynamic strength of the material, microvoids nucleate, grow and coalesce in the sample, which eventually leads to spall failure (Figure 3(d)).

Furthermore, the evolution of dislocations, HCPs, FCCs and microvoids was analyzed. As shown in Figure 4, during 0–15 ps the intense compression wave propagates from the piston into the target and activates the nucleation of dislocations at the grain boundaries. Therefore, the dislocation density and volume fraction of the HCP increase while the FCC decreases over this duration. Their contents increase significantly with the impact velocity due to the high stress state, and the denser dislocations and HCP phase enhance the spall strength of CrCoNi MEA. During 15–22.5 ps, two rarefaction waves are generated on the free surface and their

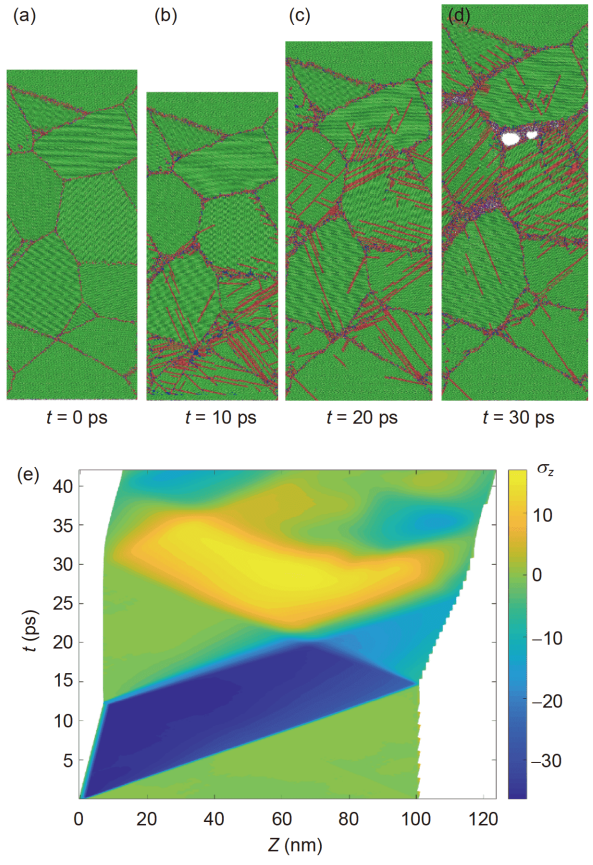


**Figure 3** Snapshots showing the microstructures of the sample at the following times. (a) 0 ps, (b) 10 ps, (c) 20 ps, and (d) 30 ps, where green and red atoms represent the FCC and HCP structures, respectively; (e) evolution of $\sigma_z$ along the shock direction in the case of $U_s$ = 600 m/s.

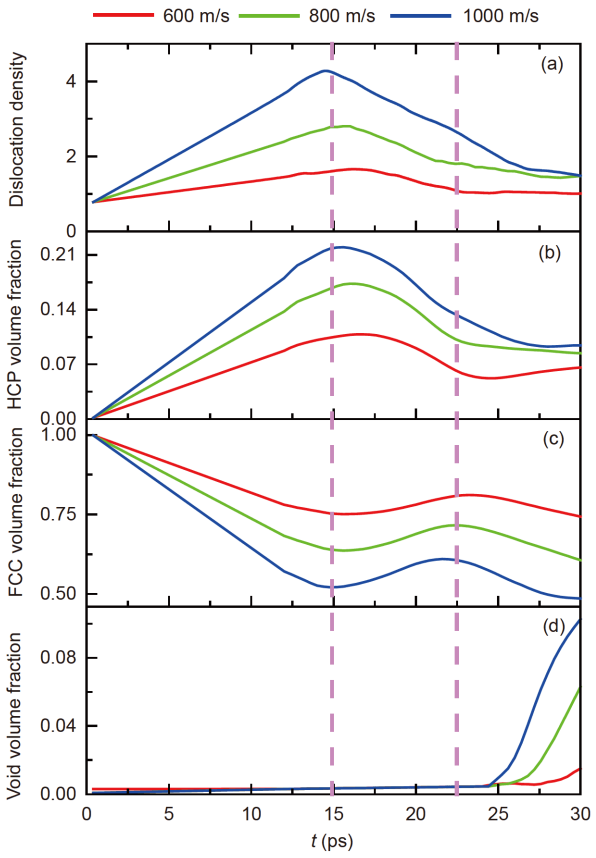


**Figure 4** The evolutions of the dislocation density (a), HCP (b), FCC (c) and microvoid volume fraction (d) in the entire system at different shock velocities, respectively.

interaction causes a tensile region in the sample. That is, the sample undergoes loading, unloading, and reverse loading, which results in a decrease in the dislocation density and the HCP and an increase in the FCC. After 22.5 ps, the dislocation density and both the HCP and FCC volume fractions decrease. This is because the system is farther away from the equilibrium state, producing severe lattice distortion and enormous disordered atoms. Some disordered atoms will become subcritical nuclei of microvoids under tensile stress, resulting in a significant increase of microvoids.

### 3.3 Intergranular nucleation

We counted the distance between the microvoids and the boundary. The detailed computational steps are as follows: first, at $t$ = 32 ps, atoms with a central symmetry parameter greater than 20 are selected as the surface atoms of microvoids in the spallation zone; then, atoms that belong to the initial grain boundary at $t$ = 32 ps are selected. Finally, the distance between atoms in these two sets is calculated. Figure 5(a) shows that microvoids prefer to nucleate at the grain boundaries, while more microvoids nucleate in grains with an increasing impact velocity. Previous work also showed that the strain rate can alter the void nucleation site from inter- [44] to intra-granular [45]. At high shock velocities, it is not quick enough to dissipate the superfluous imposed energy only forming new interface at the boundary. In addition, denser dislocations and twins provide greater opportunity to break the lattice structure and promote microvoid nucleation in the grain. Next, Region 1 (2 nm ×3 nm×15 nm) of $U_s$ = 600 m/s in Figure 5(b) and Region 2 (10 nm×10 nm×2 nm) of $U_s$ = 800 m/s in Figure 5(c) are selected as the objects to examine the microvoid nucleation in grain boundaries and grains, respectively.

As shown in Figure 6, at $t$ = 16 ps Region 1 is under compression, and the deformation and displacement of atoms

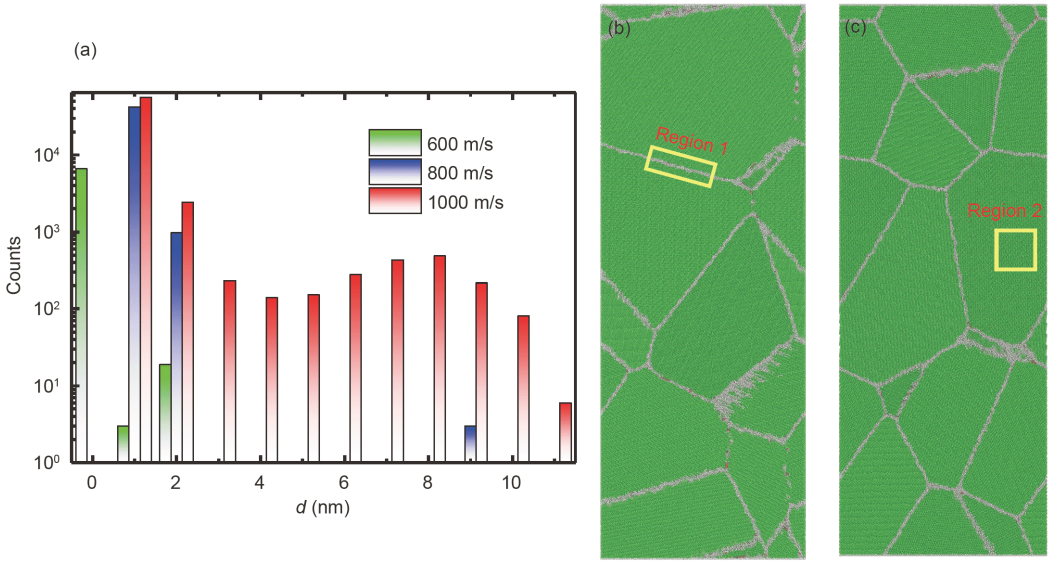


**Figure 5** (a) Distribution of the distance between the microvoid and boundary; (b), (c) representative regions in the grain boundaries and grains, respectively.

in both grains are almost consistent. Large non-affine deformation occurs in the grain boundaries due to the irregular arrangement of disordered atoms. It is under tension when $t$ = 26 ps, atoms in the upper grain undergo unloading and its displacement is small, while atoms below the grain present reverse loading. Therefore, this mismatch of atomic displacement requires coordination provided by the rotation and deformation of atoms at the grain boundary, which results in gliding of the grain boundary and exacerbates the disordered degree of the atoms at the grain boundary. At the same time, to coordinate the severe deformation in grains, new dislocations are emitted at the grain boundaries. The dislocation nucleus forms a disordered atomic layer with a thickness of the Burger's vector at the grain boundary, which leads to grain boundary broadening and structural disorder. When $t$ = 28 ps the element is in a state of high tensile stress, and some microvoids nucleate sequentially at the grain boundaries. According to classical nucleation theory, the microvoid nucleation process can be regarded as a thermodynamic process driven by stress and temperature [2,46,47]. The nucleation rate is $\dot{n} \propto \exp(-(E-W)/kT)$, where $E$ is the nucleation barrier and $W$ is the work done by loading. On one hand, the disordered atoms have relatively loose packing and a weak bond strength, so there is a lower barrier of microvoid nucleation. On the other hand, the stress concertation of the grain boundaries provides enormous energy to overcome the nucleation barrier. Therefore, high $W$ and low $E$ jointly cause microvoid nucleation.

Atoms in the grain boundary of Region 1 were divided into 50 bins along the lengthwise direction, and then the stress, deformation and element contents were calculated. As shown in Figure 7, the mean stress is approximately 11 GPa, and the Mises stress exhibits a strong fluctuation with an average stress of 16 GPa. From the viewpoint of deformation, at $t$ = 26.2 ps, strain and non-affine deformation exhibit peaks at positions $L$ = 9.2 and 12.9 nm, while the rotation angle displays a valley. That is, on the eve of microvoid nucleation, large rotation is always accompanied by low strain, and vice versa. This result is consistent with the formation process of shear band in metallic glass [48].

The region with a large strain and a relatively low rotation angle is separated by a region with a large rotation angle and a relatively low strain. The former and latter are considered soft and hard regions, respectively. This atomic motion generates an alternating sequence of soft and hard regions along the grain boundary. Analogous to the deformation of metallic glass, the volumetric strain in the grain boundaries is produced by the large tensile stress and the dilatation re-

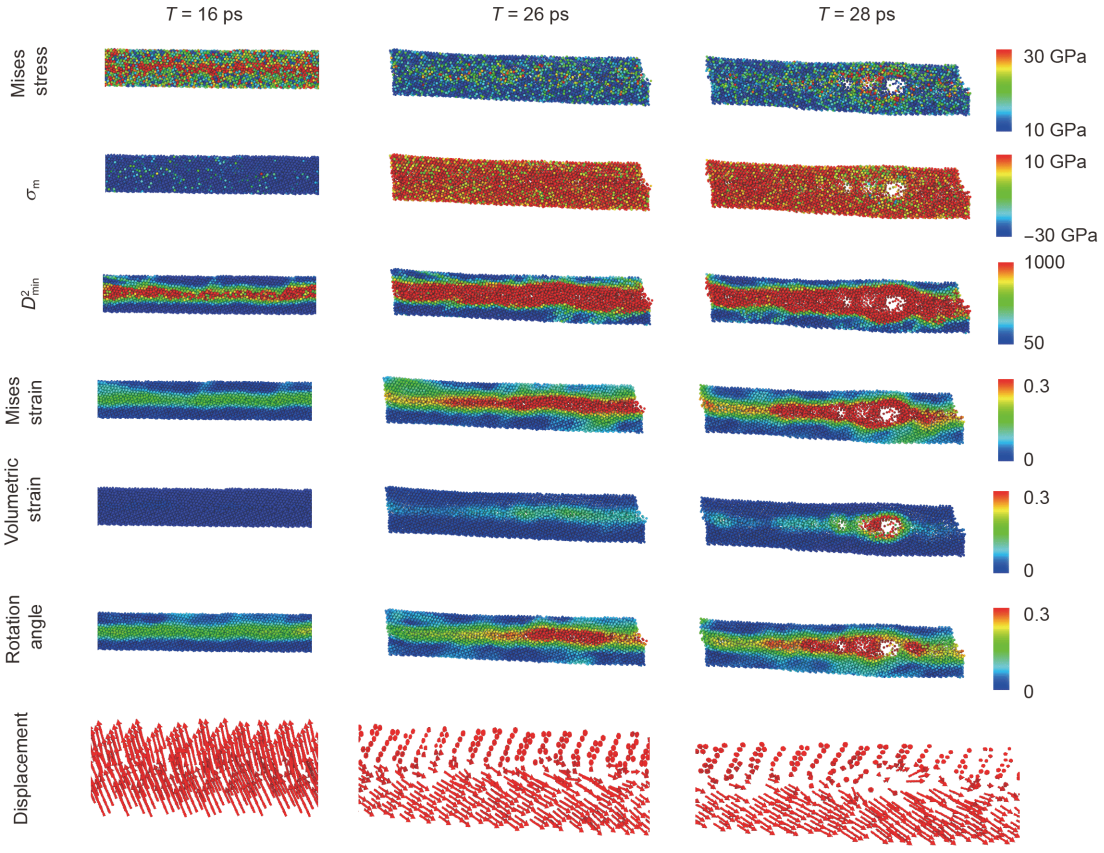


**Figure 6** Mises stress, mean stress, nonaffine deformation, Mises strain, volumetric strain, rotation angle and the displacement in Region 1 for time frames $t$ = 16, 26, and 28 ps.

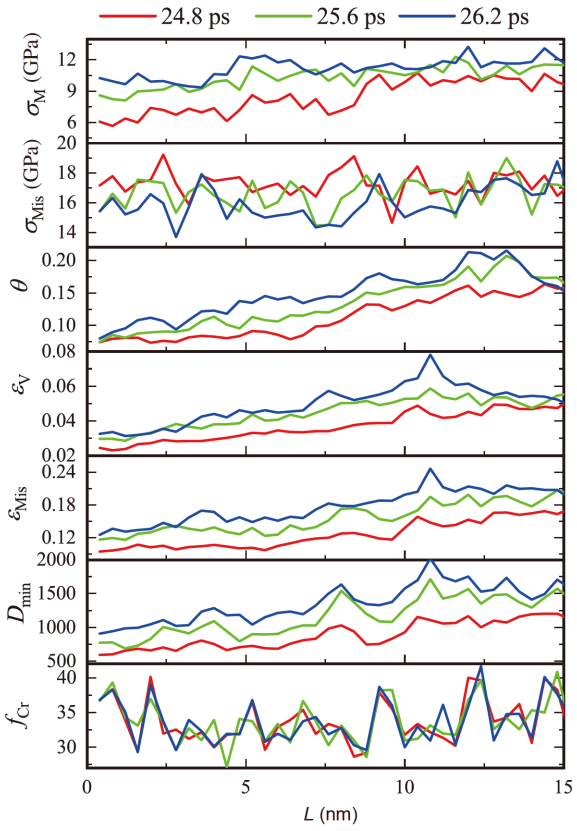


**Figure 7** Distribution of the mean stress, Mises stress, rotation angle, volumetric strain, Mises strain, nonaffine deformation and the relative Cr content along the lengthwise direction in the grain boundary of Region 1.

quired for shear transformation [49]. It is considered as microvoid nucleation when the volumetric strain in soft region is greater than the critical value. The adjacent hard region is difficult to deform and only coordinates deformation by rotation, which in turn triggers the deformation of adjacent soft region. It causes the propagation of microvoid nucleation in the grain boundary. What is more, the effect of relative content of various elements on the deformation is analyzed, where the relative content is expressed as the number of elements divided by the total atom number. The Cr-rich region corresponds to the region with a high rotation angle and low strain. Therefore, the rich-Cr region is regarded as the hard region.

To explore the effect of elements on the deformation, the average volumetric strain, shear strain, mean stress and shear stress were calculated according to the element type. As shown in Figure 8, the deformation of different elements is essentially the same during shock, while the atomic stress of Cr is greater than that of Co and Ni. That is, Cr requires a higher stress to maintain the same deformation, indicating that the bond strength between the Cr atoms and surrounding atoms is intense.

To further reveal the electronic origin of this phenomenon, we established a sample with 108 atoms using a special quasi-random structure method and alloy theoretic automated toolkit (ATAT) codes [50] and calculated the electron localization function [51]. As shown in Figure 9, the electron localization function is higher in the rich-Cr region, indicating that the electrons are concentrated. The interaction

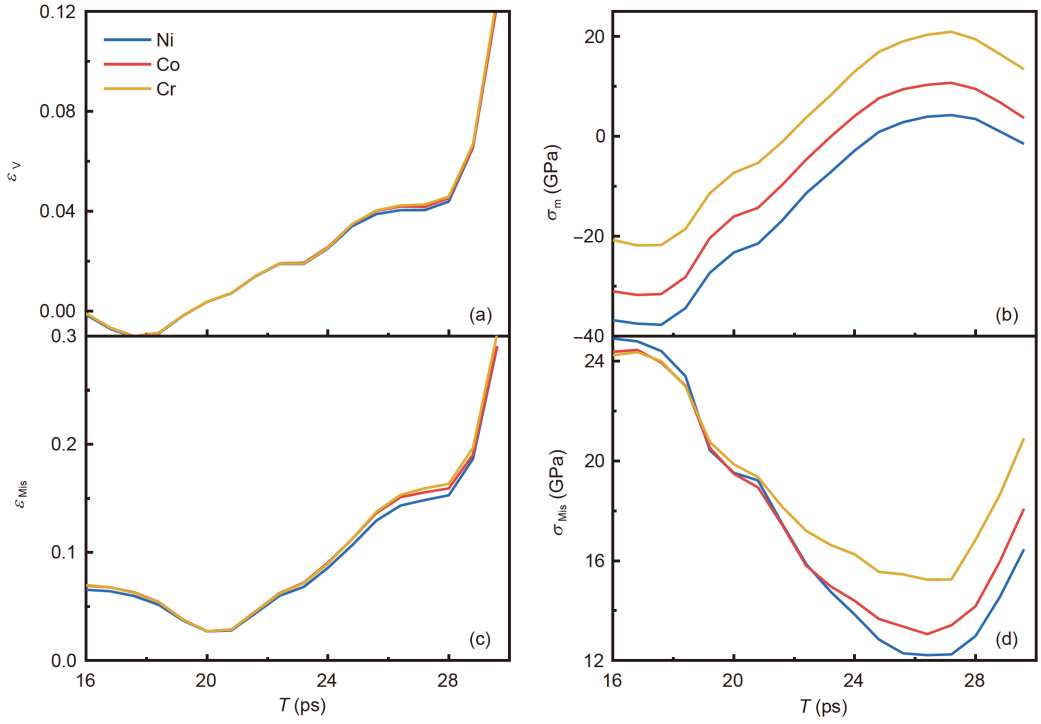


**Figure 8** The evolution of the average volumetric strain (a), mean stress (b), Mises strain (c) and Mises stress (d) for Ni, Co, and Cr, respectively.

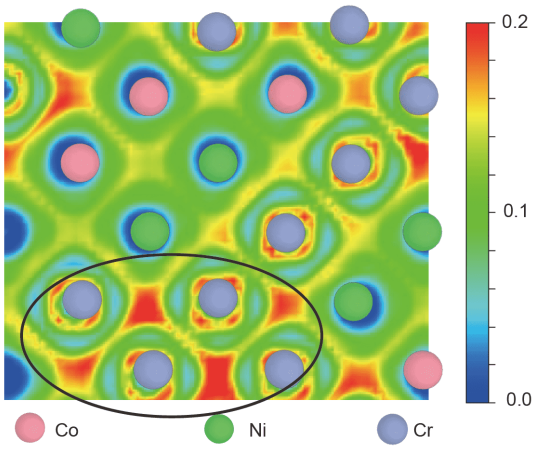


**Figure 9** Distribution of the electron localization function through the (001) plane.

between metal atoms is mainly derived from the Coulomb force between the atomic nucleus and surrounding electrons. Therefore, the agglomeration of free electrons in the rich-Cr region forms stronger metal bonds.

A detailed crystal-orbital Hamilton population (COHP) calculation was conducted to describe the bonding and antibonding contributions in the bond structure [52]. If –COHP is greater than 0, then the electron is in the bonding state; if –COHP is less than 0, then the electron is in the antibonding state. Figure 10(a) shows that the electronic energy level in the bonding state shows a wide distribution from −8 to 0.5 eV in the Cr-Cr pair; that is, all free electrons below the Fermi level are in the bonding state, and there is a strong bond. However, that of the Ni-Ni pair is far below the Fermi level (−8 – −2.3 eV), indicating that part of the free electrons remains in the antibonding state and the bond strength weakens. The bond strengths of other atomic pairs are in the range of those of Cr-Cr and Ni-Ni. These phenomena originate from the intrinsic electronic structure of the element, and the electronic structures of Cr, Co, and Ni are $3d^5 4s^1$, $3d^7 4s^2$, and $3d^8 4s^2$, respectively. It can be seen that Cr has free electrons in both the s and d orbitals, while the s and d orbitals of the Ni atoms fill up paired electrons. Furthermore, the interactions between electrons in different orbitals were calculated. The electronic energy level at the bonding state between the s-s orbitals ranges from −8 to −4 eV in all situations. The electronic attribution between the d-d orbitals of Cr-Cr at the Femi energy level is bonding, while that of Ni-Ni is antibonding; that is, the high bonding strength of Cr-Cr originates from d-d electronic interactions.

The integration of the COHP (ICOHP) curve up to the Fermi level gives the total overlap population of the bond and is a measure of the bond strength. The bond strengths of different atomic pairs were obtained by calculating the ICOHP between the nearest neighbors. As shown in Figure 11, the bond strength of Cr-Cr is the highest, which indicates that

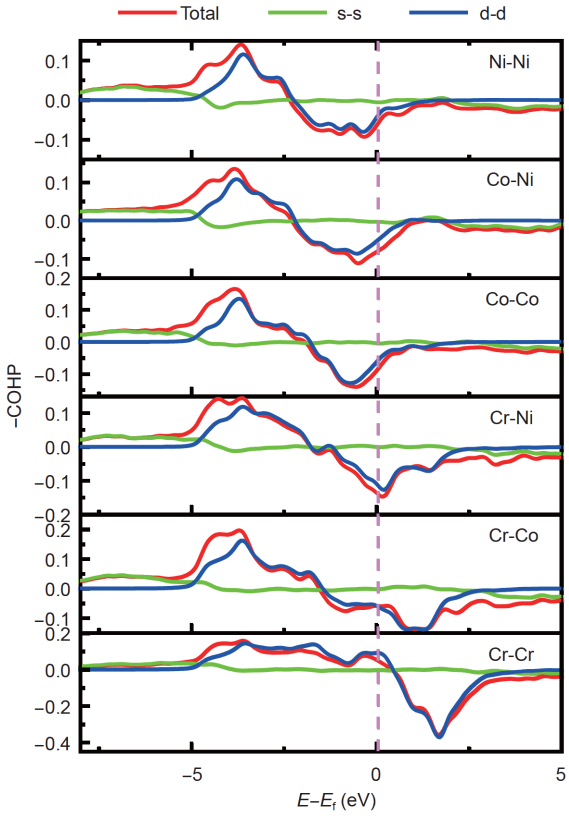


**Figure 10** (Color online) COHP for six kinds of nearest neighbor atomic pairs, where the red, green and blue lines represent the electronic interactions of the total, s and d orbitals, respectively, and 0 eV represents the Femi energy level.

the Cr-Cr bond bears a large loading in the deformation process. Compared with the rich-Cr region, the poor-Cr region is more flexible and exhibits large non-affine deformation, so microvoids prefer to nucleate in this region. There are similar results where nonaffine deformation is accompanied by substantial charge transfer in the CuZr alloy. The Cu atom is severely rearranged under shear strain due to the full d-electron states, while Zr deforms in a nearly affine manner due to the partially filled d-electron [53]. The spatial fluctuation of composition is strongly correlated with deformation and triggers the formation of a shear band [54].

This local chemical order in high/medium entropy alloys is fundamentally different from traditional solvent-solute alloys. Recent studies [38,34] have shown that the local chemical order influences the plastic deformation mechanism by varying the spatial distribution of activation barriers governing the dislocation and twin activities. This influences the selection of dislocation pathways in slip, faulting, and twinning, and increases the lattice friction to dislocation motion via a nanoscale segment detrapping mechanism. Thus, excellent mechanical property combinations can be obtained via processing to tune the local chemical order.

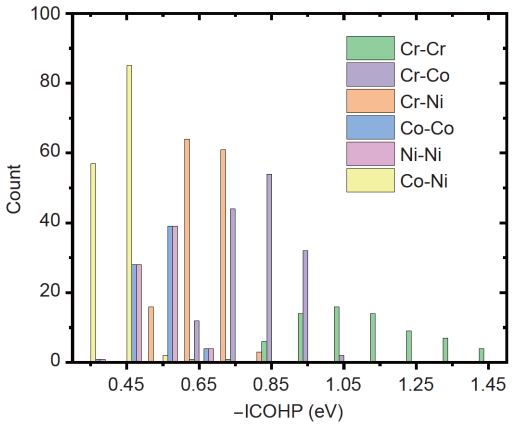


**Figure 11** Statistical distribution of ICOHP for six kinds of nearest neighbor atomic pairs.

### 3.5 Intragranular nucleation

As shown in Figure 12, at $t$ = 16 ps, atoms in Region 2 exhibit upward displacement due to the compressive stress. The propagation of dislocations causes an obvious deformation stripe along the [111] crystallographic plane. It is under tension when $t$ = 28 ps, atoms undergo unloading and reverse loading with the transition of the stress state. And a microvoid nucleates at the dislocation interaction region. Finally, the microvoids grow rapidly due to the intense tensile stress.

Now let us take a further step to examine the process from dislocation pile-up to microvoid nucleation. As shown in Figure 13(a), two partial mobile dislocations in the parallel slip planes move relatively close together at $t$ = 23.2 ps. In

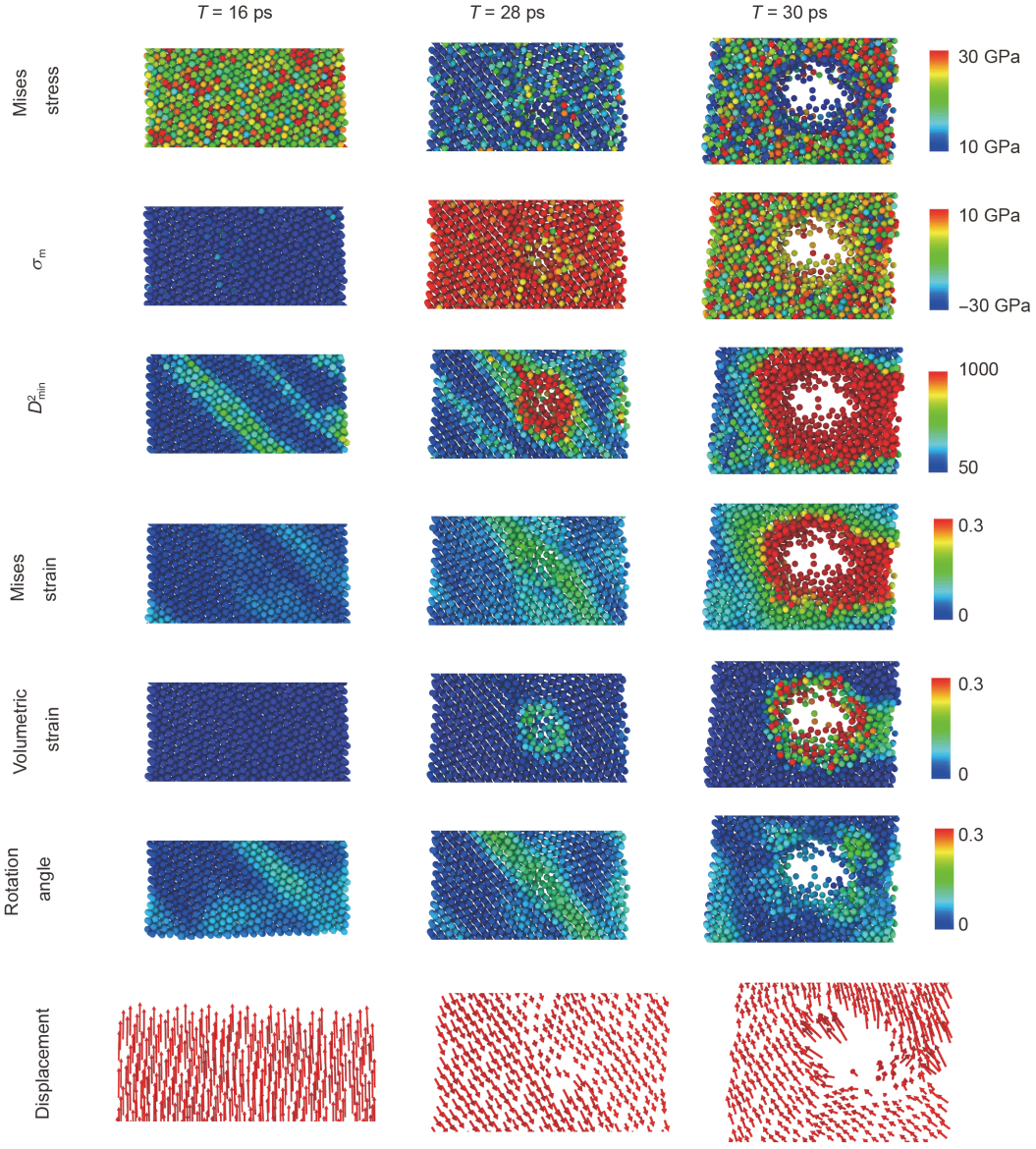


**Figure 12** Mises stress, mean stress, nonaffine deformation, Mises strain, volumetric strain, rotation angle and displacement in Region 2 for time frames $t$ = 16, 28, and 30 ps.

MEA alloys, the dislocation line is wavy and does not move smoothly due to nanoscale local chemical order heterogeneities. Therefore, the Shockley dislocation segment can encounter the same slip planes through the cross-slip, and the other segment still stays on the origin slip plane (Figure 13(i)). Then, a sessile stair-rod dislocation is produced by the following dislocation reaction: $\frac{a}{6}[\bar{2}11]+\frac{a}{6}[\bar{1}2\bar{1}] \rightarrow \frac{a}{2}[\bar{1}10]$ (Figure 13(j)), and the mobile dislocation is encircled by two sessile dislocations (Figure 13(k)). This configuration forms a Franke-like dislocation source, so many dislocations are emitted at a high stress state in a short time (Figure 13(l)). These new dislocations only move in a narrow space since the dislocation source is surrounded by dense twins that block the dislocation motion (Figure 13(c)). The piled-up dislocations cause a highly distorted lattice and markedly increase the local stored energy (Figure 13(e), (f)). These disordered structures then promote microvoid nucleation to relax the excessive stored energy by forming a new surface (Figure 13(g), (h)). These observations provide elaborate descriptions from dislocation interaction to microvoid nucleation, and clarify the roles of dislocations and twins in this process.

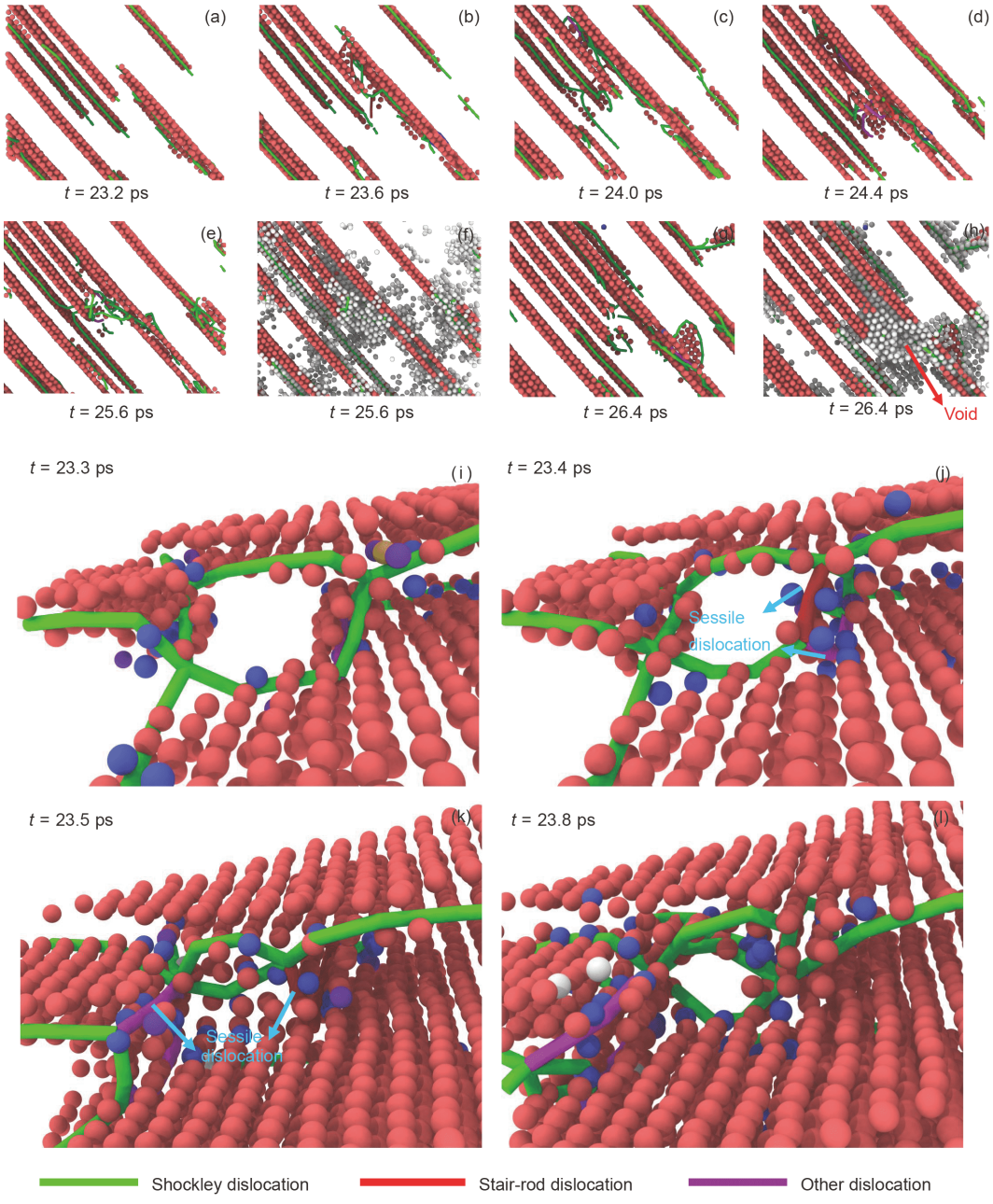


**Figure 13** (a)–(e), (g) Snapshots without the FCC phase and the disordered atoms at different times; (f), (h) snapshots without the FCC phase, where red and white atoms represent HCP and disordered atoms, respectively, and (i)–(l) elaborate layouts of the dislocation reactions.

## 4 Conclusions

The spallation processes of the CrCoNi MEA under different shock velocities were simulated, and the spall strength exhibited significant strain rate strengthening. Before microvoid nucleation, the dislocation and HCP phases first increase and then decrease during the shock compression process due to the propagation of compressive and rarefaction waves, respectively. There is a transition of microvoid nucleation sites from the boundaries to the grains with an increasing shock velocity. In the intragranular nucleation process, grain glide and dislocation nucleation make the atomic structure disordered, decreasing the nucleation energy barrier and resulting in microvoid nucleation under a high tensile stress. Moreover, the Cr-rich region exhibits an excellent resistance to microvoid nucleation, which is attributed to the agglomeration of free electrons and d-d electronic interactions, based on first principle calculations. In intergranular nucleation, the formation of a Franke-like dislocation source via the dislocation reaction leads to the pile-up of enormous dislocations in a narrow twin stripe, which markedly increases the local stored energy and promotes microvoid nucleation. These findings inaugurate a direction for searching for excellent dynamical mechanical properties by adjusting the local chemical order in the MEA.

*This work was supported by the National Key Research and Development Program of China (Grant No. 2017YFB0702003), the National Natural Science Foundation of China (NSFC) (Grant Nos. 11790292, 11972346 and 11672316), the NSFC Basic Science Center Program for "Multiscale Problems in Nonlinear Mechanics" (Grant No. 11988102), the Strategic Priority Research Program of the Chinese Academy of Sciences (Grant Nos. XDB22040302 and XDB22040303), the Key Research Program of Frontier Sciences of the Chinese Academy of Sciences (Grant No. QYZDJSSW-JSC011), and the Science Challenge Project (Grant No. TZ2018001).*

1 Hopkinson B. X. A method of measuring the pressure produced in the detonation of high, explosives or by the impact of bullets. Philos Trans R Soc London Ser A, 1914, 213: 437–456
2 Curran D. Dynamic failure of solids. Phys Rep, 1987, 147: 253–388
3 Bai Y L, Xia M, Ke F. Statistical Meso-Mechanics of Damage and Failure: How Microdamage Induces Disaster. Singapore: Springer, 2019
4 Teng H H, Jiang Z L, Progress in multi-wave structure and stability of oblique detonations. Adv Mech, 2020, 50: 202002
5 Jiao W, Chen X. Review on long-rod penetration at hypervelocity. Adv Mech, 2019, 49: 312–391
6 Tan M, Zhang X, Bao K, et al. Interface defeat of ceramic armor. Adv Mech, 2019, 49: 392–427
7 Liu X F, Tian Z L, Zhang X F, et al. "Self-sharpening" tungsten high-entropy alloy. Acta Mater, 2020, 186: 257–266
8 Bai Y L, Wang H Y, Xia M F, et al. Statistical mesomechanics of solid, linking coupled multiple space and time scales. Appl Mech Rev, 2005, 58: 372–388
9 Meyers M A, Taylor Aimone C. Dynamic fracture (spalling) of metals. Prog Mater Sci, 1983, 28: 1–96
10 Raj R, Ashby M F. Intergranular fracture at elevated temperature. Acta Metall, 1975, 23: 653–666
11 Reina C, Marian J, Ortiz M. Nanovoid nucleation by vacancy aggregation and vacancy-cluster coarsening in high-purity metallic single crystals. Phys Rev B, 2011, 84: 104117
12 Fensin S J, Escobedo J P, Gray Iii G T, et al. Dynamic damage nucleation and evolution in multiphase materials. J Appl Phys, 2014, 115: 203516
13 Marian J, Knap J, Ortiz M. Nanovoid cavitation by dislocation emission in aluminum. Phys Rev Lett, 2004, 93: 165503
14 Meyers M A, Traiviratana S, Lubarda V A, et al. The role of dislocations in the growth of nanosized voids in ductile failure of metals. JOM, 2009, 61: 35–41
15 Gurson A L. Continuum theory of ductile rupture by void nucleation and growth: Part I—Yield criteria and flow rules for porous ductile media. J Eng Mater Tech, 1977, 99: 2–15
16 Needleman A. A continuum model for void nucleation by inclusion debonding. J Appl Mech, 1987, 54: 525–531
17 Huang X, Ling Z, Dai L H. Influence of surface energy and thermal effects on cavitation instabilities in metallic glasses. Mech Mater, 2019, 131: 113–120
18 Huang X, Ling Z, Dai L H. Cavitation instabilities in bulk metallic glasses. Int J Solids Struct, 2013, 50: 1364–1372
19 Cantor B, Chang I T H, Knight P, et al. Microstructural development in equiatomic multicomponent alloys. Mater Sci Eng-A, 2004, 375-377: 213–218
20 Yeh J W, Chen S K, Lin S J, et al. Nanostructured high-entropy alloys with multiple principal elements: Novel alloy design concepts and outcomes. Adv Eng Mater, 2004, 6: 299–303
21 Gludovatz B, Hohenwarter A, Catoor D, et al. A fracture-resistant high-entropy alloy for cryogenic applications. Science, 2014, 345: 1153–1158
22 George E P, Raabe D, Ritchie R O. High-entropy alloys. Nat Rev Mater, 2019, 4: 515–534
23 Murty B S, Yeh J W, Ranganathan S, et al. High-Entropy Alloys. Elsevier, 2019
24 Shi P, Ren W, Zheng T, et al. Enhanced strength-ductility synergy in ultrafine-grained eutectic high-entropy alloys by inheriting microstructural lamellae. Nat Commun, 2019, 10: 489
25 Liang Y X, Yang X F, Ming K S, et al. *In situ* observation of transmission and reflection of dislocations at twin boundary in CoCrNi alloys. Sci China Tech Sci, 2021, 64: 407–413
26 Jia B, Liu X J, Wang H, et al. Microstructure and mechanical properties of FeCoNiCr high-entropy alloy strengthened by nano-$Y_2O_3$ dispersion. Sci China Tech Sci, 2018, 61: 179–183
27 Huang T D, Jiang L, Zhang C L, et al. Effect of carbon addition on the microstructure and mechanical properties of CoCrFeNi high entropy alloy. Sci China Tech Sci, 2018, 61: 117–123
28 Liu J P, Chen J X, Liu T W, et al. Superior strength-ductility CoCrNi medium-entropy alloy wire. Scripta Mater, 2020, 181: 19–24
29 Pu Z, Xie Z C, Sarmah R, et al. Spatio-temporal dynamics of jerky flow in high-entropy alloy at extremely low temperature. Philos Mag, 2021, 101: 154–178
30 Pu Z, Chen Y, Dai L H. Strong resistance to hydrogen embrittlement of high-entropy alloy. Mater Sci Eng-A, 2018, 736: 156–166
31 Soundararajan C K, Luo H, Raabe D, et al. Hydrogen resistance of a 1 GPa strong equiatomic CoCrNi medium entropy alloy. Corrosion Sci, 2020, 167: 108510
32 Jiang Z J, He J Y, Wang H Y, et al. Shock compression response of high entropy alloys. Mater Res Lett, 2016, 4: 226–232
33 Li Z, Zhao S, Alotaibi S M, et al. Adiabatic shear localization in the CrMnFeCoNi high-entropy alloy. Acta Mater, 2018, 151: 424–431
34 Ding Q, Zhang Y, Chen X, et al. Tuning element distribution, structure and properties by composition in high-entropy alloys. Nature, 2019, 574: 223–227
35 Zhang R, Zhao S, Ding J, et al. Short-range order and its impact on the CrCoNi medium-entropy alloy. Nature, 2020, 581: 283–287
36 Plimpton S. Fast parallel algorithms for short-range molecular dynamics. J Comput Phys, 1995, 117: 1–19
37 Hirel P. Atomsk: A tool for manipulating and converting atomic data

files. Comput Phys Commun, 2015, 197: 212–219
38 Li Q J, Sheng H, Ma E. Strengthening in multi-principal element alloys with local-chemical-order roughened dislocation pathways. Nat Commun, 2019, 10: 3563
39 Falk M L, Langer J S. Dynamics of viscoplastic deformation in amorphous solids. Phys Rev E, 1998, 57: 7192–7205
40 Stukowski A. Visualization and analysis of atomistic simulation data with OVITO—the open visualization tool. Model Simul Mater Sci Eng, 2010, 18: 015012
41 Stukowski A. Structure identification methods for atomistic simulations of crystalline materials. Model Simul Mater Sci Eng, 2012, 20: 045021
42 Stukowski A. Computational analysis methods in atomistic modeling of crystals. JOM, 2014, 66: 399–407
43 Stukowski A, Bulatov V V, Arsenlis A. Automated identification and indexing of dislocations in crystal interfaces. Model Simul Mater Sci Eng, 2012, 20: 085007
44 Zurek A K, Thissell W R, Johnson J N, et al. Micromechanics of spall and damage in tantalum. J Mater Processing Tech, 1996, 60: 261–267
45 Escobedo J P, Cerreta E K, Dennis-Koller D. Effect of crystalline structure on intergranular failure during shock loading. JOM, 2014, 66: 156–164
46 Guan P, Lu S, Spector M J B, et al. Cavitation in amorphous solids. Phys Rev Lett, 2013, 110: 1–5
47 Huang X, Ling Z, Zhang H S, et al. How does spallation microdamage nucleate in bulk amorphous alloys under shock loading? J Appl Phys, 2011, 110: 103519
48 Şopu D, Stukowski A, Stoica M, et al. Atomic-level processes of shear band nucleation in metallic glasses. Phys Rev Lett, 2017, 119: 195503
49 Zeng F, Jiang M Q, Dai L H. Dilatancy induced ductile-brittle transition of shear band in metallic glasses. Proc R Soc A, 2018, 474: 20170836
50 van de Walle A, Asta M, Ceder G. The alloy theoretic automated toolkit: A user guide. Calphad, 2002, 26: 539–553
51 Savin A, Nesper R, Wengert S, et al. ELF: The electron localization function. Angew Chem Int Ed Engl, 1997, 36: 1808–1832
52 Nelson R, Ertural C, George J, et al. LOBSTER: Local orbital projections, atomic charges, and chemical-bonding analysis from projector-augmented-wave-based density-functional theory. J Comput Chem, 2020, 41: 1931–1940
53 Lobzenko I, Shiihara Y, Iwashita T, et al. Shear softening in a metallic glass: First-principles local-stress analysis. Phys Rev Lett, 2020, 124: 085503
54 Hassani M, Lagogianni A E, Varnik F. Probing the degree of heterogeneity within a shear band of a model glass. Phys Rev Lett, 2019, 123: 195502